Simulations of a Full Three-Dimensional Packing Process and Flow-Induced Stresses in Injection Molding

Xuejuan Li, Jie Ouyang, Qiang Li, Jinlian Ren

School of Science, Northwestern Polytechnical University, Xi'an 710129, China

Received 4 August 2011; accepted 13 December 2011
DOI 10.1002/app.36648
Published online in Wiley Online Library (wileyonlinelibrary.com).

ABSTRACT: Numerical investigations of a full three-dimensional (3D) packing process and flow-induced stresses are presented. The model was constructed on the basis of a 3D nonisothermal weakly compressible viscoelastic flow model combined with extended pom-pom (XPP) constitutive and Tait state equations. A hybrid finite element method (FEM)–finite volume method (FVM) is proposed for solving this model. The momentum equations were solved by the FEM, in which a discrete elastic viscous stress split scheme was used to overcome the elastic stress instability, and an implicit scheme of iterative weakly compressible Crank–Nicolson-based split scheme was used to avoid the Ladyshenskaya–Babuška–Brezzi condition. The energy and XPP equations were solved by the FVM, in which an upwind scheme was used for the strongly convection-dominated problem of the energy equation. Subsequently, the validity of the proposed method was verified by the benchmark problem, and a full 3D packing process and flow-induced stresses were simulated. The pressure and stresses distributions were studied in the packing process and were in agreement with the results of the literature and experiments in tendency. We particularly focused on the effects of the elasticity and pressure on the flow-induced stresses. The numerical results show that normal stress differences decreased with incremental Weissenberg number and increased with incremental holding pressure. The research results had a certain reference value for improving the properties of products in actual production processes.
 J Appl Polym Sci 000: 000–000, 2012

Key words: injection molding; stress; simulations

INTRODUCTION

Injection molding is one of the most versatile polymer-processing techniques for producing plastics parts.[1] Polymer melts experience complex changes in the injection-packing process; for example, a high holding pressure induces the orientation of polymer molecules along the flow direction. The frozen-in orientation of the polymer molecules is named the *flow-induced stress* in parts. The existence of flow-induced stress is responsible for the anisotropy of the mechanical, thermal, and optical properties. Therefore, the investigation of stress distribution attracts wide attention; particularly, many researchers have used experimental methods, such as birefringence, the layer-removal method, the incremental hole-drilling method, and the photoelasticity method to determine the stress distribution.[2–4] However, these experiments could hardly trace the transient change of flow-induced stress in the packing process. In general, computer simulation and experimentation are complementary to each other. Hence, it is necessary to study the flow characteristics and the flow-induced stress distribution of the packing stage with computer simulation.

So far, numerical simulations of the flow-induced stress have mainly been done with the compressible Leonov model[5–7] and Phan–Thien–Tanner (PTT) constitutive equation[8] based on the generalized Hele–Shaw (GHS) flow model in the packing or postfilling stage. In these simulations, the flow-induced stress associated with the Leonov model is related to flow-induced birefringence through the linear stress–optical rule in literatures[6,7] so that the predicted birefringence can be compared with the experimental results. Cao et al.[8] provided a semianalysis method to simulate the flow-induced stress distribution on the basis of the PTT constitutive equation in injection molding. In terms of the flow model, although GHS has been extensively applied in various research because of its advantages of simplified calculation, it cannot do anything to capture some information, such as fountain flow and the kinematics in areas where the shear and extensional deformations contribute significantly to the stress field.[9,10] Fortunately, full three-dimensional (3D) models simulation can generate complementary and more detailed information related to the problems mentioned previously. Some numerical simulations in full 3D have been developed for the filling stage in recent

Correspondence to: J. Ouyang (jieouyang@nwpu.edu.cn).
Contract grant sponsors: National Basic Research Program of China, National Natural Science Foundation of China; contract grant number: 2012CB025903, 10871159.

years.[10–16] For example, the finite element method (FEM) was first used[10,12] to simulate the 3D filling stage, and then, the Petrov–Galerkin (PG) method[13,14] was proposed to prevent potential numerical instabilities in the FEM. In the finite volume method (FVM) formulation, a high-resolution interface-capturing method[15] and a 3D two-phase model[16] that avoids the use of the ghost fluid method are used to simulate the injection-molding filling stage. However, full 3D simulation of the packing stage in injection molding has been rather scarce until now. Most simulations have been based on the GHS model,[17,18] and only Kang et al.[19] gave an isothermal 3D example in the literature, in which penalty formulation was employed to simulate the postfilling of injection molding. In terms of the stress model, the Leonov model was derived from classical elastic network potential energy theory, the PTT model was developed on the basis phenomenological theory, and the theoretical foundation of the extended pom-pom (XPP) model[20,21] was the molecular theory of rheology. To sum up the previously analysis, the XPP model can provide a good fitting to the rheology of polymer melts.

In this study, we mainly focused on the numerical investigation of the complex rheological behavior in the 3D packing stage and on flow-induced stress evolution. In our numerical simulations, the 3D nonisothermal weakly compressible viscoelastic flow was considered, and it was governed by the XPP model combined with the viscosity model of Cross and Williams–Landel–Ferry (WLF). Meanwhile, the Tait state equation was introduced to deal with compressibility of the polymer melt. To our knowledge, a full 3D packing process incorporating the XPP model for flow-induced stresses has not yet been studied.

However, it is extremely difficult to numerically simulate a full 3D packing process because of flow-induced stress. First, the computation complexity and Ladyshenskaya–Babuška–Brezzi (LBB) condition are two great difficulties. To overcome these difficulties, the fractional step algorithm is introduced into the FEM formulation, and it uncouples the pressure term from the velocity components.[22] Actually, the fractional step algorithm can avoid the LBB condition only when the time step exceeds some threshold value. Unfortunately, the high viscosity of the polymer requires the time step to be very small for the explicit scheme. Therefore, an implicit scheme has to be employed, and one needs to introduce an iterative process to avoid solving three momentum equations simultaneously. Second, the high specific heat capacity of the polymer results in the energy equation being a strongly convection-dominated diffusion equation. To resolve this kind of problem in FEM, various stabilization techniques, such as the streamline upwind, PG, and streamline upwind PG methods, need to be employed. However, those stabilization techniques increase the difficulty of spatial discretization. So we considered introducing the upwind scheme (US) in the FVM to solve this problem. Third, the lack of ellipticity of the momentum equation is an important problem in viscoelastic flow analysis. Some methods, such as the explicitly elliptic momentum equation formulation,[23] elastic viscous stress split formulation,[24] and discrete elastic viscous stress split (DEVSS) scheme,[25] have been studied to solve this problem. DEVSS has been proven to be very effective.[26,27] Fourth, the stresses equations exhibit convection-dominated characteristics as the Weissenberg number (We) increases, so the stresses were solved in the FVM formulation and the energy equation.

To sum up the previous arguments, a hybrid FEM–FVM was proposed to simulate the flow-induced stresses on the basis of the XPP model. The proposed method was motivated by the DEVSS technique adopted for momentum equations, and the equations were discretized by the iterative implicit weakly compressible Crank–Nicolson-based split (WCNBS) scheme in the FEM formulation. The energy and XPP equations were discretized in the FVM formulation in which an US was used for the energy equation. The proposed hybrid scheme was applied to simulate the full 3D packing process with flow-induced stresses. Particularly, the influences of the holding pressure and the elasticity on the first and second normal stress differences (N_1 and N_2, respectively) are discussed.

MATHEMATICAL MODEL

Governing equations

The flow of polymer melts in the packing stage is governed by the conservation of mass, momentum and energy equations, together with a constitutive equation. They are given as follows:

$$\rho_t + \nabla \cdot (\rho \mathbf{u}) = 0 \tag{1}$$

$$\rho \mathbf{u}_t + \rho \mathbf{u} \cdot \nabla \mathbf{u} = \eta_s \nabla^2 \mathbf{u} - \nabla \cdot p + \nabla \cdot \boldsymbol{\tau} + \eta_s / 3 \nabla (\nabla \cdot \mathbf{u}) \tag{2}$$

$$C_p(\rho T_t + \rho \mathbf{u} \cdot \nabla T) = \kappa \nabla^2 T + \eta_s \dot{\gamma}^2 + \boldsymbol{\tau} : \nabla \mathbf{u} \tag{3}$$

where the subscript t denotes the time derivative, ρ is the density, $\mathbf{u}$ is the velocity vector, p is the pressure, η_s is the Newtonian (solvent) contribution of the total viscosity [$\eta(T, \dot{\gamma}, p)$, where $\dot{\gamma}$ is the shearing rate], $\boldsymbol{\tau}$ is the elastic stress tensor, C_p is the specific heat, κ is the thermal conductivity, T is the temperature.

When the polymeric (elastic) contribution η_p of the total viscosity $\eta(T, \dot{\gamma}, p)$ is introduced and

the coefficient of thermal expansion is defined as $\beta = \eta_s/\eta$, the governing eqs. (1)–(3) can made be nondimensional via

$$\mathbf{x}^* = \mathbf{x}/L, \mathbf{u}^* = \mathbf{u}/U, t^* = tU/L, \rho^* = \rho/\rho_r, p^* = p/(\rho_r U^2),$$
$$T^* = T/T_r, \ \boldsymbol{\tau}^* = \boldsymbol{\tau}L/(\eta_r U), \eta^*(T, \dot{\gamma}, p) = \eta(T, \dot{\gamma}, p)/\eta_r$$

where $\mathbf{x}$ is the space vector, L is the length scale, U is the velocity scale, ρ_r is the density scale, T_r is the temperature scale, and η_r is the viscosity scale. As a matter of convenience, the asterisk is omitted and $\eta(T, \dot{\gamma}, p)$ is written as η. Also, the governing eqs. (1)–(3) can be written as follows:

$$\rho_t + \nabla(\rho\mathbf{u}) = 0 \tag{4}$$

$$\rho\mathbf{u}_t + \rho\mathbf{u}\nabla\mathbf{u} = \eta\beta/\mathrm{Re}\nabla^2\mathbf{u} - \nabla p + 1/\mathrm{Re}\nabla\boldsymbol{\tau} + \eta\beta/(3\mathrm{Re})\nabla(\nabla\mathbf{u}) \tag{5}$$

$$\mathrm{Pe}(\rho T_t + \rho\mathbf{u}\nabla T) = \nabla^2 T + \mathrm{Br}\beta\eta\dot{\gamma}^2 + \mathrm{Br}\boldsymbol{\tau} : \nabla\mathbf{u} \tag{6}$$

where Re is the Reynolds number ($\mathrm{Re} = \rho_r UL/\eta_r$), Pe is the Péclet number ($\mathrm{Pe} = \rho_r C_p UL/\kappa$), and Br is the Brinkman number [$\mathrm{Br} = \eta_r U^2/(\kappa T_r)$].

XPP model

In this study, the single equation version of the XPP model in multi-mode form[28,29] was used. The constitutive equation for the XPP model is

$$f(\lambda, \boldsymbol{\tau})\boldsymbol{\tau} + \lambda_{0,b}\overset{\nabla}{\boldsymbol{\tau}} + G_0[f(\lambda, \boldsymbol{\tau}) - 1]\mathbf{I} + \frac{\alpha}{G_0}\boldsymbol{\tau}\cdot\boldsymbol{\tau} = 2\lambda_{0b}G_0\mathbf{D} \tag{7}$$

where λ_{0b} is the orientation relaxation time, $\mathbf{I}$ is the unit tensor, $\mathbf{D}$ is the rate of deformation tensor [$\mathbf{D} = \frac{1}{2}(\nabla\mathbf{u} + (\nabla\mathbf{u})^T)$], G_0 is the linear relaxation modulus, α is the anisotropy parameter, the symbol "∇" represents the following upper-convected derivative

$$\overset{\nabla}{\boldsymbol{\tau}} = \frac{\partial\boldsymbol{\tau}}{\partial t} + \mathbf{u}\cdot\nabla\boldsymbol{\tau} - (\nabla\mathbf{u})^T\boldsymbol{\tau} - \boldsymbol{\tau}\nabla\mathbf{u} \tag{8}$$

and the function $f(\lambda,\boldsymbol{\tau})$ is given by

$$f(\lambda, \boldsymbol{\tau}) = 2\frac{\lambda_{0b}}{\lambda_{0s}}e^{\nu(\lambda-1)}\left(1 - \frac{1}{\lambda}\right) + \frac{1}{\lambda^2}\left(1 - \frac{\alpha tr(\boldsymbol{\tau}\cdot\boldsymbol{\tau})}{3G_0^2}\right) \tag{9}$$

where λ_{0s} is the backbone stretch relaxation time, ν is inversely proportional to the number of arms (q), $\nu = 2/q$, tr(·) is the trace of tensor and λ is the backbone stretch and the expression is related to $\boldsymbol{\tau}$ as follows in the XPP model

$$\lambda = \sqrt{1 + \frac{|tr(\boldsymbol{\tau})|}{3G_0}} \tag{10}$$

Thus, the polymeric tensor $\boldsymbol{\tau}$ is defined by eqs. (7)–(10).

We define $\eta_p = G_0\lambda_{0b}$ and $\varepsilon = \lambda_{0s}/\lambda_{0b}$, where ε is the ratio of the stretch to the orientation relaxation time. This shows that small values of ε correspond to highly entangled backbones. The constitutive equation possesses features of the Giesekus model because a nonzero N_2 is predicted when α is not equal to zero. The parameter ν in the exponential term was incorporated into the stretch relaxation time, to remove the discontinuity from the gradient of the extensional viscosity.

The nondimensional form of eq. (7) is as follows:

$$f(\lambda,\boldsymbol{\tau})\boldsymbol{\tau} + \mathrm{We}\overset{\nabla}{\boldsymbol{\tau}} + \frac{(1-\beta)}{We}[f(\lambda,\boldsymbol{\tau}) - 1]\mathbf{I} + \frac{\alpha We}{1-\beta}\boldsymbol{\tau}\cdot\boldsymbol{\tau} = 2(1-\beta)\mathbf{D} \tag{11}$$

where Weissenberg number $We = \lambda_{0b}U/L$.

Viscosity model

Because of the high-temperature sensitivity of the polymer melt viscosity, the Cross model is the most appropriate model to study the problem of nonisothermal polymer melt flow and was chosen to assess the total viscosity of the polymer melt. In addition, the Cross approach was selected to better adjust the temperature and pressure sensitivities of the zero-shear-rate viscosity.[30]

The Cross model has seven parameters and its expression is as follows

$$\eta(T, \dot{\gamma}, p) = \frac{\eta_0(T, p)}{1 + (\eta_0\dot{\gamma}/\boldsymbol{\tau}^*)^{1-n}} \tag{12}$$

where $\eta_0(T,p)$ is the melt viscosity under zero-shear-rate conditions, $\boldsymbol{\tau}^*$ is the model constant that shows the shear stress rate from which the pseudoplastic behavior of the melt starts, and n is the model constant that symbolizes the pseudoplastic behavior slope of the melt as $1 - n$.

The WLF expression is considered to determine the zero-shear viscosity (η_0) of the melt

$$\eta_0 = D_1 \exp\left(\frac{-A_1\left(T - \hat{T}\right)}{A_2\left(T - \hat{T}\right)}\right) \tag{13}$$

where

$$\hat{T} = D_2 + D_3 p$$

and

$$A_2 = \tilde{A}_2 + D_3 p$$

where $\hat{T}$ is the glass-transition temperature of the melt, A_1 is the model constant that shows the temperature dependence of the melt glass-transition temperature under zero-shear-rate conditions, D_1 is the model constant that registers the melt viscosity under zero-shear-rate conditions at the melt glass-transition temperature and at atmospheric pressure, D_2 is the model constant that registers the glass-transition temperature, D_3 is the model constant that symbolizes the variation of the glass-transition temperature of the melt according to the pressure, p is the pressure, and $\tilde{A}_2$ is a model parameter that depends on the type of polymer melt that has been considered.

State equation

We introduce a Pressure-Volume-Temperature (PVT) state equation to satisfy the completeness of governing equations. Tait equation is usually considered as the classical empirical equation and is capable of describing both the liquid and solid regions.[31] Tait equation can be represented as follows:

$$\frac{1}{\rho} = V(p,T) = V_0(T)\left\{1 - C\ln\left[1 - \frac{P}{B(T)}\right]\right\} + V_t(T,p) \tag{14}$$

where $V(p,T)$ is the specific volume.

The related terms can be expressed as follows:

$$V_0(T) = \begin{cases} b_{1m} + b_{2m}(T - b_5) & \text{if } T > T_t \\ b_{1s} + b_{2s}(T - b_5) & \text{if } T < T_t \end{cases} \tag{15}$$

$$B(T) = \begin{cases} b_{3m}\exp[-b_{4m}(T - b_5)] & \text{if } T > T_t \\ b_{3s}\exp[-b_{4s}(T - b_5)] & \text{if } T < T_t \end{cases} \tag{16}$$

$$V_t(T,p) = \begin{cases} 0 & \text{if } T > T_t \\ b_7\exp[b_8(T - b_5) - b_9 p] & \text{if } T < T_t \end{cases} \tag{17}$$

where $C = 0.0894$ is a universal constant; b_1, b_2, b_3, b_4, b_5, b_6, b_7, b_8, and b_9 are material constants; the subscripts m and s identify the melt and solid, respectively; $T_t = b_5 + b_6 p$ is the glass-transition temperature of the melt, where b_5 indicates the transition temperature under zero-pressure conditions and b_6 indicates the linear variation of the transition temperature with increasing pressure; $V_0(T)$ is the isothermal specific volume under zero-pressure conditions; $B(T)$ expresses the degree of influence of pressure on the specific volume; and $V_t(T,p)$ is introduced to account for the volume decrease due to crystallization. For the amorphous polymers, the parameter b_{1m} equals b_{1s} so that $V_0(t)$ is continuous at $T = b_5 = T_t$ ($p = 0$). So, in the nonisothermal melt flow, we adopted the two-region Tait state equation.

NUMERICAL METHODS

We give some statements before giving the numerical methods. Because of the compressibility of fluid, ρ is also a variable in governing equations. For compressible flows, one must discretize the variable ρ like **u** or p. However, because the compressibility of a weakly compressible fluid is very small in normal conditions, ρ is not discretized in space, and the ρ space derivations are ignored in governing equations. Furthermore, within a typical time subinterval $[t_n, t_{n+1}]$ with $\Delta t = t_{n+1} - t_n$, we adopt the ρ at t_n time to calculate the others variables at t_{n+1} time. Then, we calculate ρ of each point at t_{n+1} time. So, the number of variables of governing equations for a weakly compressible fluid is the same as that for an incompressible fluid.

DEVSS scheme

In this study, the DEVSS formulation was used to overcome the elastic stress instability problem. By introducing **D,** the DEVSS is constructed on the basis of eq. (5) as follows:

$$\frac{\partial(\rho\mathbf{u})}{\partial t} + \nabla(\rho\mathbf{u}\mathbf{u}) = -\nabla p + \frac{\eta}{\mathrm{Re}}\nabla^2\mathbf{u} - \frac{2(1-\beta)\eta}{\mathrm{Re}}\nabla\mathbf{D} + \frac{(1-4/3\beta)\eta}{\mathrm{Re}}\nabla(\nabla\mathbf{u}) + \frac{1}{\mathrm{Re}}\nabla\boldsymbol{\tau} \tag{18}$$

$$\underline{\mathbf{D}} - \mathbf{D} = 0 \tag{19}$$

WCNBS scheme for FEM formulation

WCNBS scheme

On the basis of the Tait state equation, an implicit numerical scheme of WCNBS was used to avoid the LBB condition. Before proceeding with the split procedure of the fractional step scheme, we considered the discretization of eq. (5) in the time domain within a typical time subinterval $[t_n, t_{n+1}]$, which gave us the form of the Wilson–θ method as follows:

$$\frac{\rho^n}{\Delta t}\left(\mathbf{u}^{n+1} - \mathbf{u}^n\right) = -(\nabla p)^{n+\theta} - \nabla(\rho\mathbf{u}\mathbf{u})^{n+\theta_1} + \left(\frac{\eta}{\mathrm{Re}}\nabla^2\mathbf{u}\right)^{n+\theta_2} + \left[\frac{(1-4/3\beta)\eta}{\mathrm{Re}}\nabla(\nabla\mathbf{u})\right]^{n+\theta_2} - \left[\frac{2(1-\beta)\eta}{\mathrm{Re}}\nabla\mathbf{D}\right]^{n+\theta_D} + \frac{1}{\mathrm{Re}}\nabla\boldsymbol{\tau}^{n+\theta_\tau} \tag{20}$$

where $0 < \theta, \theta_1, \theta_2, \theta_D, \theta\boldsymbol{\tau} \leq 1$. To construct the fractional step scheme, $\theta \neq 0$ for the pressure gradient term is required. When $\theta = \theta_1 = \theta_2 = \theta_D = \theta_\tau = 0.5$,

eq. (20) has the second-order accuracy, which was adopted in this study for the Crank–Nicolson scheme.

On the basis of different expressions of pressure, fractional step algorithms can be classified into two different forms: the incremental type[32] and the nonincremental type.[33,34] Guermond et al.[33] proved that the incremental-type fractional step algorithm had better stability than the nonincremental-type fractional step algorithm. So, we adopted the -type fractional step algorithm in this study.

With the introduction of an intermediate variable ($\mathbf{u}'$) and $A^{n+\theta} = \theta A^{n+1} + (1-\theta)A^n$, eq. (20) for the Crank–Nicolson scheme was split into two parts (Crank–Nicolson-based splitting) as follows:

$$\left(\frac{\rho^n}{\Delta t} - \frac{\eta^{n+\theta_2}}{\mathrm{Re}}\theta_2\nabla^2\right)(\mathbf{u}' - \mathbf{u}^n) = -\nabla p^n - \nabla(\rho\mathbf{u}\mathbf{u})^{n+\theta_1} + \frac{\eta^{n+\theta_2}}{\mathrm{Re}}(\nabla^2\mathbf{u}^n) + \left[\frac{(1-4/3\beta)\eta}{\mathrm{Re}}\nabla(\nabla\mathbf{u})\right]^{n+\theta_2} - \left[\frac{2(1-\beta)\eta}{\mathrm{Re}}\nabla\mathbf{D}\right]^{n+\theta_D} + \frac{1}{\mathrm{Re}}\nabla\boldsymbol{\tau}^{n+\theta_\tau} \quad (21)$$

$$\left(\frac{\rho^n}{\Delta t} - \frac{\eta^{n+\theta_2}}{\mathrm{Re}}\theta_2\nabla^2\right)(\mathbf{u}^{n+1} - \mathbf{u}') = -\theta\nabla(p^{n+1} - p^n) \quad (22)$$

Taking the divergence of the vector in eq. (22) and omitting the high-order term, we obtained

$$\frac{\rho^n}{\Delta t}\nabla(\mathbf{u}^{n+1} - \mathbf{u}') = -\theta\nabla(p^{n+1} - p^n) \quad (23)$$

For nonisothermal weakly compressible flow, on basis of the ρ dependence from the pressure and temperature and the chain-derivation rule, the time derivative of ρ is given as follows:

$$\frac{\partial p}{\partial t} = \frac{\partial\rho}{\partial p}\frac{\partial p}{\partial t} + \frac{\partial\rho}{\partial T}\frac{\partial T}{\partial t} \quad (24)$$

where $\partial\rho/\partial p = \rho_\alpha$ and $\partial\rho/\partial T = -\rho_\delta$ can be obtained from eq. (14) and α and δ are the coefficients of isothermal compressibility and thermal expansion. The substitution of eq. (4) and eq. (21) into eq. (20) results in the pressure equation, which is given as follows:

$$\left(\frac{\partial\rho}{\partial p}\frac{1}{\Delta t} - \theta\Delta t\nabla^2\right)(p^{n+1} - p^n) = -\rho^n\nabla\mathbf{u}' - \frac{\partial\rho}{\partial T}\frac{T^{n+1} - T^n}{\Delta t} \quad (25)$$

Equations (21), (25), and (22) are the first, second, and third steps, respectively, of the WCNBS scheme. However, because the second term on the right-hand side of eq. (25) contains t_{n+1}, which must be known before eq. (25) is calculated, eq. (25) is divided into two parts to calculate the pressure:

$$\left(\frac{\partial\rho}{\partial p}\frac{1}{\Delta t} - \theta\Delta t\nabla^2\right)(p^{n+1} - p^n) = -\rho^n\nabla\mathbf{u}' \quad (26)$$

$$\left(\frac{\partial\rho}{\partial p}\frac{1}{\Delta t} - \theta\Delta t\nabla^2\right)(p^{n+1} - p^n) = -\frac{\partial\rho}{\partial T}\frac{T^{n+1} - T^n}{\Delta t} \quad (27)$$

Before calculating eq. (27), one must update p_n with eq. (26) and introduce the implicit scheme of energy equation to calculate the temperature.

FEM spatial discretization

In the FEM formulation, the variables $\mathbf{u}$, p, $\boldsymbol{\tau}$, and $\mathbf{D}$ are spatially approximated with the standard finite element shape functions ($\mathbf{N}_u$, $\mathbf{N}_p$, $\mathbf{N}_\tau$, and $\mathbf{N_D}$), which are based on four-node tetrahedral elements and expressed in terms of their nodal values ($\overline{\mathbf{u}}$, $\overline{p}$, $\overline{\boldsymbol{\tau}}$, and $\overline{\mathbf{D}}$, respectively) as follows:

$$\mathbf{u} = \mathbf{N}_{\mathbf{u}j}\overline{\mathbf{u}}_j,\ p = \mathbf{N}_{pj}\overline{p}_j, \mathbf{D} = \mathbf{N}_{Dj}\overline{\mathbf{D}}_j,\ \boldsymbol{\tau} = \mathbf{N}_{\tau j}\overline{\boldsymbol{\tau}}_j\ j = 1,2,3,4 \quad (28)$$

where $\mathbf{N_u}$, $\mathbf{N}_p$, $\mathbf{N}_\tau$, and $\mathbf{N}_D$ are first-order linear shape functions ($\mathbf{N_u} = \mathbf{N}_p = \mathbf{N}_\tau = \mathbf{N}_D = \mathbf{N}$). With the standard Galerkin finite element discretization, the weak forms of eqs. (19), (21), (22), (26), and (27) can be written as follows:

$$\mathbf{M}\overline{\mathbf{D}}^{n+1} = \mathbf{H}\overline{\mathbf{u}}^{n+1} \quad (29)$$

$$\left(\frac{\rho^n}{\Delta t}\mathbf{M} + \frac{\eta^{n+\theta_2}}{\mathrm{Re}}\theta_2\mathbf{K}_1\right)(\overline{\mathbf{u}}' - \overline{\mathbf{u}}^n) = -\rho^n\mathbf{C}\overline{\mathbf{u}}^{n+\theta_1} - \frac{\eta^{n+\theta_2}}{\mathrm{Re}}\mathbf{K}_1\overline{\mathbf{u}}^n - \mathbf{G}\overline{p}^n - \frac{(1-4/3\beta)\eta^{n+\theta_2}}{\mathrm{Re}}\mathbf{K}_2\overline{\mathbf{u}}^{n+\theta_1} + \frac{2(1-\beta)\eta^{n+\theta_D}}{\mathrm{Re}}\mathbf{K}_3\overline{\mathbf{D}}^{n+\theta_D} - \frac{1}{\mathrm{Re}}\mathbf{K}_3\overline{\boldsymbol{\tau}}^{n+\theta_\tau} \quad (30)$$

$$\left(\frac{\rho^n}{\Delta t}\mathbf{M} + \frac{\eta^{n+\theta_2}}{\mathrm{Re}}\theta_2\mathbf{K}_1\right)(\overline{\mathbf{u}}^{n+1} - \overline{\mathbf{u}}') = -\theta\mathbf{G}(\overline{p}^{n+1} - \overline{p}^n) \quad (31)$$

$$\left(\frac{\partial\rho}{\partial p}\frac{1}{\Delta t}\mathbf{M} + \theta\Delta t\mathbf{K}_1\right)(\overline{p}^{n+1} - \overline{p}^n) = -\rho^n\mathbf{J}\overline{\mathbf{u}}' \quad (32)$$

$$\left(\frac{\partial\rho}{\partial p}\frac{1}{\Delta t}\mathbf{M} + \theta\Delta t\mathbf{K}_1\right)(\overline{p}^{n+1} - \overline{p}^n) = -\frac{\partial\rho}{\partial T}\frac{1}{\Delta t}\mathbf{M}(\overline{T}^{n+1} - \overline{T}^n) \quad (33)$$

And all of the previous matrices are formulated as follows

$$\mathbf{M}=\int_{\Omega}\mathbf{N}^{T}\mathbf{N}d\Omega,\mathbf{K}_{1}=\int_{\Omega}(\nabla\mathbf{N})^{T}(\nabla\mathbf{N})d\Omega,$$
$$\mathbf{K}_{2}=\int_{\Omega}(\nabla\mathbf{N})^{T}(\nabla\cdot\mathbf{N})d\Omega,\mathbf{K}_{3}=\int_{\Omega}(\nabla\cdot\mathbf{N})^{T}\mathbf{N}d\Omega,$$
$$\mathbf{C}=\int_{\Omega}\mathbf{N}^{T}\mathbf{u}(\nabla\mathbf{N})d\Omega,\mathbf{G}=\int_{\Omega}\mathbf{N}^{T}(\nabla\mathbf{N})d\Omega,$$
$$\mathbf{J}=\int_{\Omega}\mathbf{N}^{T}(\nabla\cdot\mathbf{N})d\Omega,\mathbf{H}=1/2\int_{\Omega}\mathbf{N}^{T}I_{0}\mathbf{S}\mathbf{N}d\Omega \quad (34)$$

where $\mathbf{N}^T$ is the transposition of $\mathbf{N}$, d is the differential, Ω is the domain of integration, $\mathbf{I}_0$ = diag(2,2,2,1,1,1),

$$\mathbf{S}=\begin{bmatrix}\partial/\partial x & 0 & 0 & \partial/\partial y & 0 & \partial/\partial z\\ 0 & \partial/\partial y & 0 & \partial/\partial x & \partial/\partial z & 0\\ 0 & 0 & \partial/\partial z & 0 & \partial/\partial y & \partial/\partial x\end{bmatrix}^{T}.$$

Temperature and stress solvers for the FVM formulation

The energy and stress equations were discretized by the FVM on nonstaggered meshes, and all quantities were stored on the same nodes. Nodes for the physical quantities were in the center of the controlling volume, limited by the dashes.

Energy equation discretization

The discretization of eq. (6) can be written as follows:

$$a_pT_p=a_ET_E+a_WT_W+a_NT_N+a_ST_S+a_RT_R+a_LT_L+S_T \quad (35)$$

where S_T is the source term in the energy equation, and the coefficients a_E, a_W, a_N, a_S, a_R, a_L, and a_P can be expressed as follows:

$$\begin{aligned}a_E&=D_eA(|P_e|)+\max(-F_e,0),\\ a_W&=D_wA(|P_w|)+\max(F_w,0),\\ a_N&=D_nA(|P_n|)+\max(-F_n,0),\\ a_S&=D_sA(|P_s|)+\max(F_s,0),\\ a_R&=D_rA(|P_r|)+\max(-F_r,0),\\ a_L&=D_lA(|P_l|)+\max(F_l,0),\\ a_p&=a_E+a_W+a_N+a_S+\mathrm{Pe}\rho\frac{\Delta x\Delta y\Delta z}{\Delta t}.\end{aligned}$$

where P_e, P_s, P_w, P_n, P_r, and P_l are the Péclet numbers on the cell faces; F_e, F_s, F_w, F_n, F_r, and F_l are the flux values of the cell faces; A denote an operator and it's expression is given, $A(|P_\Delta|)=1$; and D_e, D_s, D_w, D_n, D_r, and D_l are the diffuse derivatives on the cell faces. The form $A(|P_\Delta|)$ can be different according to the method by which the convection terms are discretized. The US was adopted in this study for strongly convection-dominated problems, so that $A(|P_\Delta|)=1$, and all of the previous coefficients were formulated as follows:

$$\begin{aligned}&F_e=\mathrm{Pe}(\rho u)_{fe}\Delta y\Delta z,D_e=\frac{\Delta y\Delta z}{x_E-x_P},\\ &P_e=\frac{F_e}{D_e};F_w=\mathrm{Pe}(\rho u)_{fw}\Delta y\Delta z,D_w=\frac{\Delta y\Delta z}{x_P-x_W},P_w=\frac{F_w}{D_w};\\ &F_n=\mathrm{Pe}(\rho v)_{fn}\Delta x\Delta z,D_n=\frac{\Delta x\Delta z}{y_N-y_P},\\ &P_n=\frac{F_n}{D_n};F_s=\mathrm{Pe}(\rho v)_{fs}\Delta x\Delta z,D_s=\frac{\Delta x\Delta z}{y_P-y_S},P_s=\frac{F_s}{D_s};\\ &F_r=\mathrm{Pe}(\rho w)_{fr}\Delta x\Delta y,D_r=\frac{\Delta x\Delta y}{z_E-z_P},\\ &P_r=\frac{F_r}{D_r};F_l=\mathrm{Pe}(\rho w)_{fl}\Delta x\Delta y,D_l=\frac{\Delta x\Delta y}{z_P-z_L},P_l=\frac{F_l}{D_l}.\end{aligned} \quad (36)$$

Constitutive equation discretization

The constitutive equation can be written as the following form by a generalized quantity (ϕ):

$$m\frac{\partial\phi}{\partial t}\nabla\cdot(m\mathbf{u}\phi)-\nabla\cdot(\Gamma\nabla\phi)=S_\phi \quad (37)$$

The constants and functions in eq. (37) are defined in Table I. τ_{xx}, τ_{yy}, τ_{zz}, τ_{xy}, τ_{xz} and τ_{yz} are the components of tensor $\boldsymbol{\tau}$ in Table I, and the subscript x, y, z denote the directions. Similarly, the discretization of the constitutive equation can be written as the following form:

$$a_p^{\tau}\phi_p=a_E^{\tau}\phi_E+a_W^{\tau}\phi_W+a_N^{\tau}\phi_N+a_S^{\tau}\phi_S+a_R^{\tau}\phi_R+a_L^{\tau}\phi_L+S_\phi \quad (38)$$

where S_ϕ is the source term in the constitutive equation and the coefficients a_E^{τ}, a_W^{τ}, a_N^{τ}, a_S^{τ}, a_R^{τ}, a_L^{τ}, and a_P^{τ} can be expressed as follows:

$$\begin{aligned}&a_E^{\tau}=\mathrm{We}\max(-Fe,0),a_W^{\tau}=\mathrm{We}\max(Fw,0),\\ &a_N^{\tau}=\mathrm{We}\max(-Fn,0),\\ &a_S^{\tau}=\mathrm{We}\max(Fs,0),a_R^{\tau}=\mathrm{We}\max(-Fr,0),\\ &a_L^{\tau}=\mathrm{We}\max(F_l,0),\\ &a_p^{\tau}=a_E^{\tau}+a_W^{\tau}+a_N^{\tau}+a_S^{\tau}+a_R^{\tau}+a_L^{\tau}+We\frac{\Delta x\Delta y\Delta z}{\Delta t}.\end{aligned}$$

Numerical steps

In terms of the numerical method design, to enhance the computational efficiency, an iterative procedure was introduced for the convective terms of the momentum equations. The detailed numerical steps for solving the nonisothermal viscoelastic packing stage are summarized as follows:

Step 1

Provide the initial velocity ($\overline{\mathbf{u}}^0$), initial pressure ($\overline{p}^0$), initial density ($\overline{\rho}^0$), initial stress ($\overline{\boldsymbol{\tau}}^0$), and initial

TABLE I
Constants and Functions in eq. (37)

Equation	Φ	m	Γ	S_ϕ
τ_{xx}	τ_{xx}	We	0	$-f(\lambda,\tau)\tau_{xx} + 2\mathrm{We}\frac{\partial u}{\partial x}\tau_{xx} + 2\mathrm{We}\frac{\partial u}{\partial y}\tau_{xy} + 2\mathrm{We}\frac{\partial u}{\partial z}\tau_{xz}$ $-\frac{\alpha\mathrm{We}}{1-\beta}\left(\tau_{xx}^2+\tau_{xy}^2+\tau_{xz}^2\right) - \frac{1-\beta}{\mathrm{We}}(f(\lambda,z)-1) + 2(1-\beta)\frac{\partial u}{\partial x} - \frac{2}{3}\left(\frac{\partial u}{\partial x}+\frac{\partial v}{\partial y}+\frac{\partial w}{\partial z}\right)$
τ_{xy}	τ_{xy}	We	0	$\mathrm{We}\frac{\partial v}{\partial x}\tau_{xx} + \mathrm{We}\left(\frac{\partial u}{\partial x}+\frac{\partial v}{\partial y}\right)\tau_{xy} + \mathrm{We}\frac{\partial v}{\partial z}\tau_{xz} + \mathrm{We}\frac{\partial u}{\partial y}\tau_{yy} + \mathrm{We}\frac{\partial u}{\partial z}\tau_{yz}$ $-f(\lambda,\tau)\tau_{xy} - \frac{\alpha\mathrm{We}}{1-\beta}\left(\tau_{xx}\tau_{xy}+\tau_{xy}\tau_{yy}+\tau_{xz}\tau_{yz}\right) + (1-\beta)\left(\frac{\partial u}{\partial y}+\frac{\partial v}{\partial x}\right)$
τ_{xz}	τ_{xz}	We	0	$\mathrm{We}\frac{\partial w}{\partial x}\tau_{xx} + \mathrm{We}\frac{\partial w}{\partial y}\tau_{xy} + \mathrm{We}\left(\frac{\partial w}{\partial z}+\frac{\partial u}{\partial x}\right)\tau_{xz} + \mathrm{We}\frac{\partial u}{\partial y}\tau_{yz} + \mathrm{We}\frac{\partial u}{\partial z}\tau_{zz}$ $-f(\lambda,\tau)\tau_{xz} - \frac{\alpha\mathrm{We}}{1-\beta}\left(\tau_{xx}\tau_{xy}+\tau_{xy}\tau_{yy}+\tau_{xz}\tau_{yz}\right) + (1-\beta)\left(\frac{\partial u}{\partial z}+\frac{\partial w}{\partial x}\right)$
τ_{yy}	τ_{yy}	We	0	$-f(\lambda,\tau)\tau_{yy} + 2\mathrm{We}\frac{\partial v}{\partial x}\tau_{xy} + 2\mathrm{We}\frac{\partial v}{\partial y}\tau_{yy} + 2\mathrm{We}\frac{\partial v}{\partial z}\tau_{yz}$ $-\frac{\alpha\mathrm{We}}{1-\beta}\left(\tau_{xy}^2+\tau_{yy}^2+\tau_{yz}^2\right) - \frac{1-\beta}{\mathrm{We}}(f(\lambda,z)-1) + 2(1-\beta)\frac{\partial v}{\partial y} - \frac{2}{3}\left(\frac{\partial u}{\partial x}+\frac{\partial v}{\partial y}+\frac{\partial w}{\partial z}\right)$
τ_{yz}	τ_{yz}	We	0	$\mathrm{We}\frac{\partial w}{\partial x}\tau_{xy} + \mathrm{We}\frac{\partial v}{\partial x}\tau_{xz} + \mathrm{We}\frac{\partial w}{\partial y}\tau_{yy} + \mathrm{We}\left(\frac{\partial w}{\partial z}+\frac{\partial v}{\partial y}\right)\tau_{yz} + \mathrm{We}\frac{\partial u}{\partial z}\tau_{zz}$ $-f(\lambda,\tau)\tau_{yz} - \frac{\alpha\mathrm{We}}{1-\beta}\left(\tau_{xy}\tau_{xz}+\tau_{yy}\tau_{yz}+\tau_{yz}\tau_{zz}\right) + (1-\beta)\left(\frac{\partial v}{\partial z}+\frac{\partial w}{\partial y}\right)$
τ_{zz}	τ_{zz}	We	0	$-f(\lambda,\tau)\tau_{zz} + 2\mathrm{We}\frac{\partial w}{\partial x}\tau_{xz} + 2\mathrm{We}\frac{\partial w}{\partial y}\tau_{yz} + 2\mathrm{We}\frac{\partial w}{\partial z}\tau_{zz}$ $-\frac{\alpha\mathrm{We}}{1-\beta}\left(\tau_{xz}^2+\tau_{yz}^2+\tau_{zz}^2\right) - \frac{1-\beta}{\mathrm{We}}(f(\lambda,z)-1) + 2(1-\beta)\frac{\partial v}{\partial y} - \frac{2}{3}\left(\frac{\partial u}{\partial x}+\frac{\partial v}{\partial y}+\frac{\partial w}{\partial z}\right)$

temperature ($\overline{T}^0$) on the grid points and then set the time-step number to $n = 0$.

Step 2

Let $\overline{\mathbf{u}}_0^{n+1} = \overline{\mathbf{u}}^n$, $\overline{\boldsymbol{\tau}}_0^{n+1} = \overline{\boldsymbol{\tau}}^n$, and set the iterations to $i = 1$.

Step 3

Calculate $\overline{\varphi}_i^{n+\theta} = (1-\theta)\overline{\varphi}^n + \theta\overline{\varphi}_{i-1}^{n+1}$ and then calculate $\eta^{n+\theta}(\overline{\mathbf{u}}^{n+\theta})$ according to eq. (12) at each grid point. Then, substitute them into eq. (30) to calculate $\overline{\mathbf{u}}'$.

Step 4

Calculate $\partial\rho/\partial P$ and then obtain $\overline{p}^{n+1}$ by calculating the pressure from eq. (32).

Step 5

Use $\overline{p}^{n+1}$ and $\overline{\mathbf{u}}'$ to calculate $\overline{\mathbf{u}}_i^{n+1}$ according to eq. (31).

Step 6

Calculate $\overline{\mathbf{D}}^{n+1}$ according to eq. (29).

Step 7

Update $\overline{\mathbf{u}}_i^{n+\theta} = (1-\theta)\overline{\mathbf{u}}^n + \theta\overline{\mathbf{u}}_i^{n+1}(\varphi = \mathbf{u}, \boldsymbol{\tau})$, and calculate $\overline{\boldsymbol{\tau}}_i^{n+1}$ according to eq. (38).

Step 8

Check for the convergence of the ith iteration process by $|\overline{\varphi}_i^{n+1} - \overline{\varphi}_{i-1}^{n+1}|\infty$ (where $|\cdot|\infty$ is the infinite norm, $\varphi = \mathbf{u}, \boldsymbol{\tau}$). If $|\overline{\varphi}_i^{n+1} - \overline{\varphi}_{i-1}^{n+1}|\infty < \varepsilon$ ($\varepsilon = 10{-}6$), $\overline{\varphi}^{n+1} = \overline{\varphi}_i^{n+1}$, otherwise $i = i + 1$ and go to step 3.

Step 9

Calculate $\eta(\overline{\mathbf{u}}^{n+1})$ according to eq. (12) at each grid point. Use the values of $\overline{\mathbf{u}}^{n+1}$, $\overline{\boldsymbol{\tau}}^{n+1}$, and $\overline{\rho}^n$ to calculate them on the cell faces, and then calculate $\overline{T}^{n+1}$ by eq. (33).

Step 10

Update p^n by p^{n+1}, which is obtained from step 5, and calculate $\partial\rho/\partial P$. Then calculate $\partial\rho/\partial T$ and calculate p^{n+1} by eq. (31).

TABLE II
Cross–WLF Viscosity Model and Thermal Properties Parameters of ABS 780

Parameter	Value	Parameter	Value
n	2.89×10^{-3}	D_3 (K/Pa)	0.0
τ^* (Pa)	3.480×10^4	A_1	24.96
D_1 (Pa s)	8.62×10^{10}	$\tilde{A}_2$ (K)	51.6
D_2 (K)	3.7315×10^2	κ (W/m °C)	0.192
C_p (J kg^{-1} °C^{-1})	1.847×10^3		

TABLE III
Tait State Equation Parameters of ABS 780

Parameter	Value	Parameter	Value	Parameter	Value
$b_{1,m}$ (m^3/kg)	9.748×10^{-4}	$b_{1,s}$ (m^3/kg)	9.748×10^{-4}	b_5 (K)	3.6175×10^2
$b_{2,m}$ (m^3 kg^{-1} K^{-1})	6.274×10^{-7}	$b_{2,s}$ (m^3 kg^{-1} K^{-1})	3.102×10^{-7}	b_6 (K/Pa)	2.881×10^{-7}
$b_{3,m}$ (Pa)	1.764×10^8	$b_{3,s}$ (Pa)	2.417×108		
$b_{4,m}$ (1/K)	4.556×10^{-3}	$b_{4,s}$ (1/K)	4.575×10^{-3}		

Step 11

Use $\overline{p}^{n+1}$ and $\overline{T}^{n+1}$ to calculate $\overline{\rho}^{n+1}$ according to eq. (7) at the per mesh point.

Step 12

Let $n = n + 1$ and go to step 2 until the termination condition is satisfied.

On the basis of the previous calculating process, with a VC++6.0 programming environment, develop the computing programming for the full 3D viscoelastic packing process analysis. The calculation is implemented on a personal computer.

NUMERICAL RESULTS

Viscoelastic planar Poiseuille flow

In this section, the benchmark problems of flows through a planar channel are modeled on the basis of Oldroyd-B and XPP models. The polymer acrylonitrile–butadiene–styrene (ABS) 780 was chosen as the flow fluid (Kumho Chemicals Inc, Seoul, Korea). The material parameters of ABS 780, which were obtained from the materials database of Moldflow software, are shown in Tables II and III, respectively.

The dimensionless parameters were taken as follows: Re = 0.00624, Pe = 90,456.825, Br = 7849.58, q = 2.0, $\beta = 1/9.0$, $\alpha = 0.15$, and $\varepsilon = 1/3.0$. The schematic of the planar Poiseuille flow is shown in Figure 1. The length/width ratio was 6 : 1. Time-step termination was ensured when the L_2-norm relative maximum difference vector between the solution approximations over two successive time steps fell later than a set threshold 10^{-6}, where L_2-norm denotes the square root of the squares sum of the vector's components.

The fully developed flow was imposed at the inlet given in eq. (39). No-slip conditions were imposed on the solid boundaries. At the exit, the pressure was set to zero, and homogeneous Neumann boundary conditions were imposed for the stresses. The temperatures $T = 500$ given at the inlet and solid boundaries temperatures $T_w = 490$ were imposed on the solid boundaries:

$$u = \frac{3}{8}(1 - 4y^2), \quad v = 0 \tag{39}$$

The analytical solutions for the stresses were[35]

$$\tau_{xx} = 2We(1-\beta)\left(\frac{\partial u}{\partial y}\right)^2, \tau_{xy} = (1-\beta)\frac{\partial u}{\partial y} \tag{40}$$

To test the accuracy of the method, the normal and shear stresses at steady state were compared with the analytical solutions. Figure 2 shows the comparison between the analytical and numerical solutions of τ_{xx} and τ_{xy} at We = 0.5. It can be seen that numerical solutions superimposed each other and showed very good agreement with the analytical solutions. Furthermore, the stresses of Poiseuille flow were the same on the bases of different constitutive equations, such as those from the Oldroyd-B and XPP models.

The contour distribution of pressure is shown in Figure 3(a), in which the contours of the pressure were almost all straight lines. The results prove that the presented WCNBS method could avoid the LBB condition for weakly compressible polymer melt flows. Figure 3(b,c) shows the contour distributions of normal and shear stresses. It can be seen that the contours were smooth, even near the exit; this could attributed to the use of the DEVSS scheme.

Figure 4 shows the normal stress cross section along $x = 3.0$ at the center line of the channel for increasing We. From Figure 4, we see that the

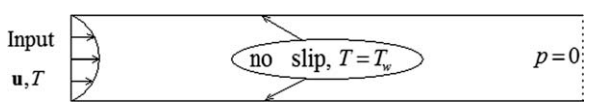

Figure 1 Planar channel geometry in the two-dimensional plane.

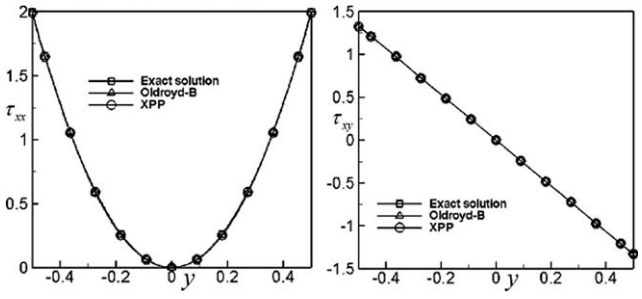

Figure 2 Comparison of the stresses between the analytical and numerical solutions.

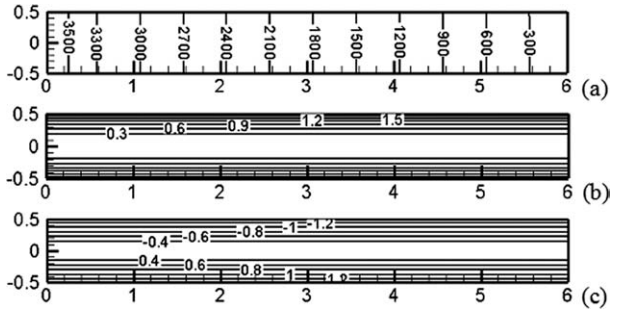

Figure 3 Contour distributions of the (a) pressure and stresses (b) τ_{xx} and (c) τ_{xy}.

numerical results compared very well with the analytical solutions.

Full 3D packing process and flow-induced stresses analysis

To study the evolution and distribution of the flow-induced stresses of the packing process, a numerical simulation was performed for a cuboid mold cavity ($10 \times 5 \times 1$), as shown in Figure 5. The material parameters were the same as those discussed earlier. Three reference points [P_1 (2.5, 0.5, 0.5), P_2 (2.5, 5.1, 0.5), and P_3 (2.5, 9.5, 0.5)] are given in Figure 5, at which point P_1 is near the gate. The XPP model was used to simulate the flow-induced stresses of the packing process.

Initial and boundary conditions

In injection molding, the packing process starts after the filling stage, so the initial conditions of the packing stage are the end status of the filling stage, in which the pressure and temperature values are used for the packing stage. Because the filling time is usually short and the temperature changes little, the temperature is not considered in the filling stage.

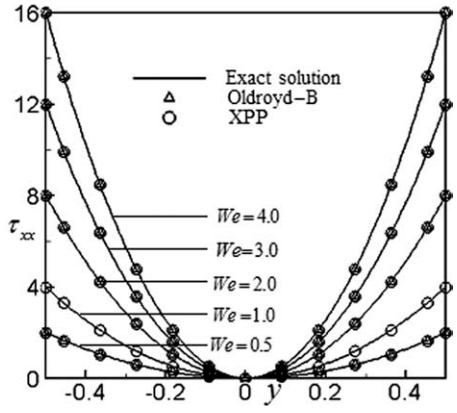

Figure 4 Cross sections of τ_{xx} along $x = 3.0$ with increasing We.

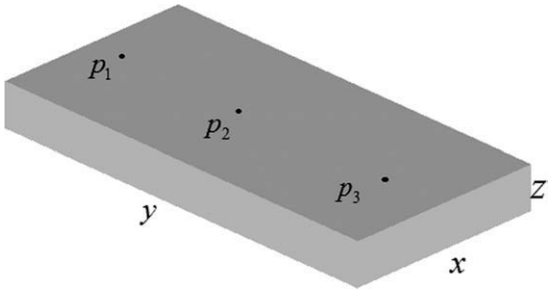

Figure 5 Sketch map and computational area of the mold.

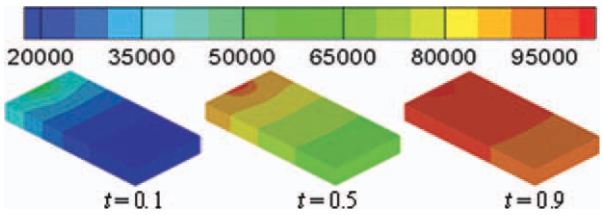

Figure 6 Pressure contour distributions at different times with $p_{\text{holding}} = 105$. [Color figure can be viewed in the online issue, which is available at wileyonlinelibrary.com.]

For the temperature boundary conditions, $T = 513$ was given at the gate, $T_w = 323$ was imposed on the solid boundaries, and Neumann boundary conditions were imposed at the symmetric axis. Pressure was imposed at the gate (p_{holding}).

Pressure distribution and discussion

The pressure contours at different times are shown in Figure 6, from which we see that the pressure values were digressive from the gate to the end of the cavity and increased everywhere as the time increased. Figure 7 shows the pressure evolutions of the reference points at different times with $p_{\text{holding}} =$

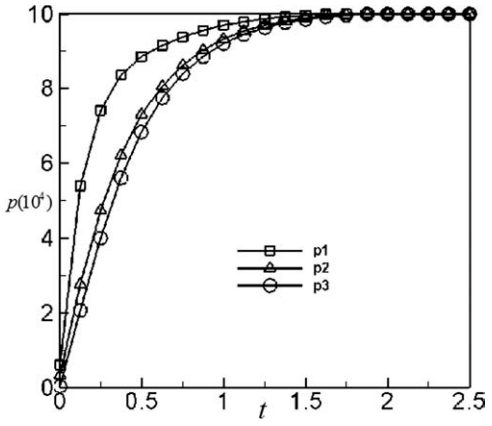

Figure 7 Pressure evolutions of the reference points at different times with $p_{\text{holding}} = 105$.

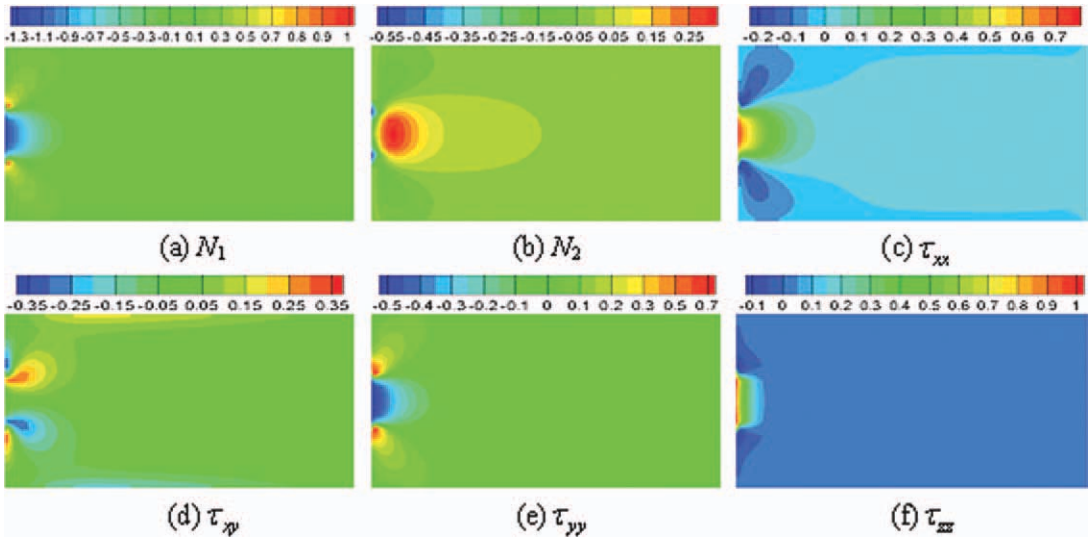

Figure 8 Stress distributions of the $z = 0.5$ midplane at $t = 0.5$ with We = 1.0 and $p_{\text{holding}} = 105$. [Color figure can be viewed in the online issue, which is available at wileyonlinelibrary.com.]

105. It can be seen that the pressure values of all of the reference points reached the holding pressure at different times, and the reference point near the gate reached the holding pressure earlier than the other reference points. The results mentioned previously were in good agreement with those in the literature.[10,11]

Flow-induced stresses distribution and discussion

Figures 8 and 9 show the flow-induced stress distributions at different midplanes at dimensionless time (t) = 0.5 with We = 1.0 and $p_{\text{holding}} = 105$. The components of the stress τ_{xz} and τ_{yz} are not be given in Figure 8 and τ_{xy} and τ_{xz} are not given in Figure 9 because they were almost zero. It can be seen from Figures 8 and 9 that N_1 and N_2 and every component of stress were symmetric about the midline. The stress distributions showed the greatest difference near the gate, and N_1 and N_2 were maximum near the gate, where there existed complex shear and normal forces. The N_1 and N_2 profiles of the $z = 0.5$ and $x = 2.5$ midplanes at different times and y values with We = 1.0 and $p_{\text{holding}} = 105$ are shown in Figures 10 and 11. We could see clearly that the absolute values of N_1 and N_2 decreased first and increased afterward with increasing time. Moreover, the distribution tendencies of N_1 at different positions of flow direction were coincident, and so were those of N_2.

Comparisons of the results between the simulation and the experiment

To make a comparison with the experimental results, the linear stress–optical rule[6] was adopted to calculate the flow-induced birefringence, which was in the x–y plane:

$$\Delta n = n_x - n_y = C\left(\left(\tau_{xx} - \tau_{yy}\right)^2 + 4\tau_{xy}^2\right)^{1/2} \tag{41}$$

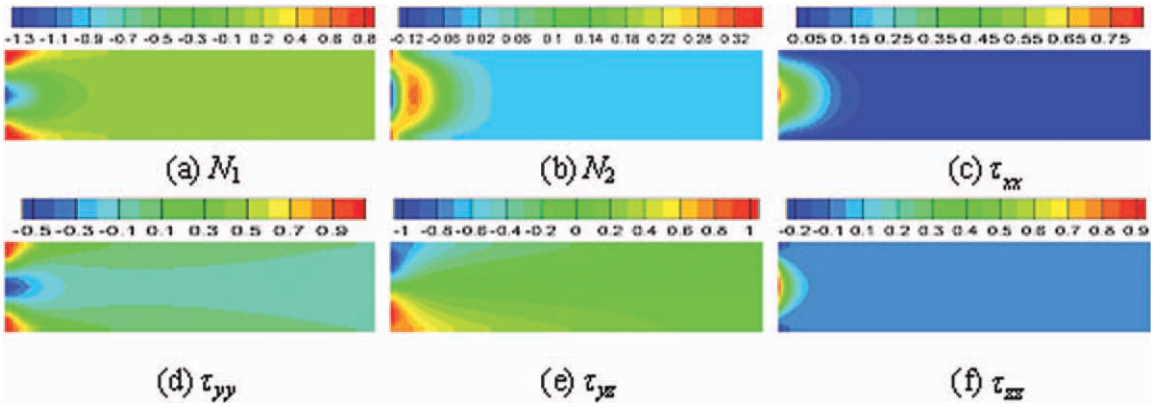

Figure 9 Stress distribution of the $x = 2.5$ midplane at $t = 0.5$ with We = 1.0 and $p_{\text{holding}} = 105$. [Color figure can be viewed in the online issue, which is available at wileyonlinelibrary.com.]

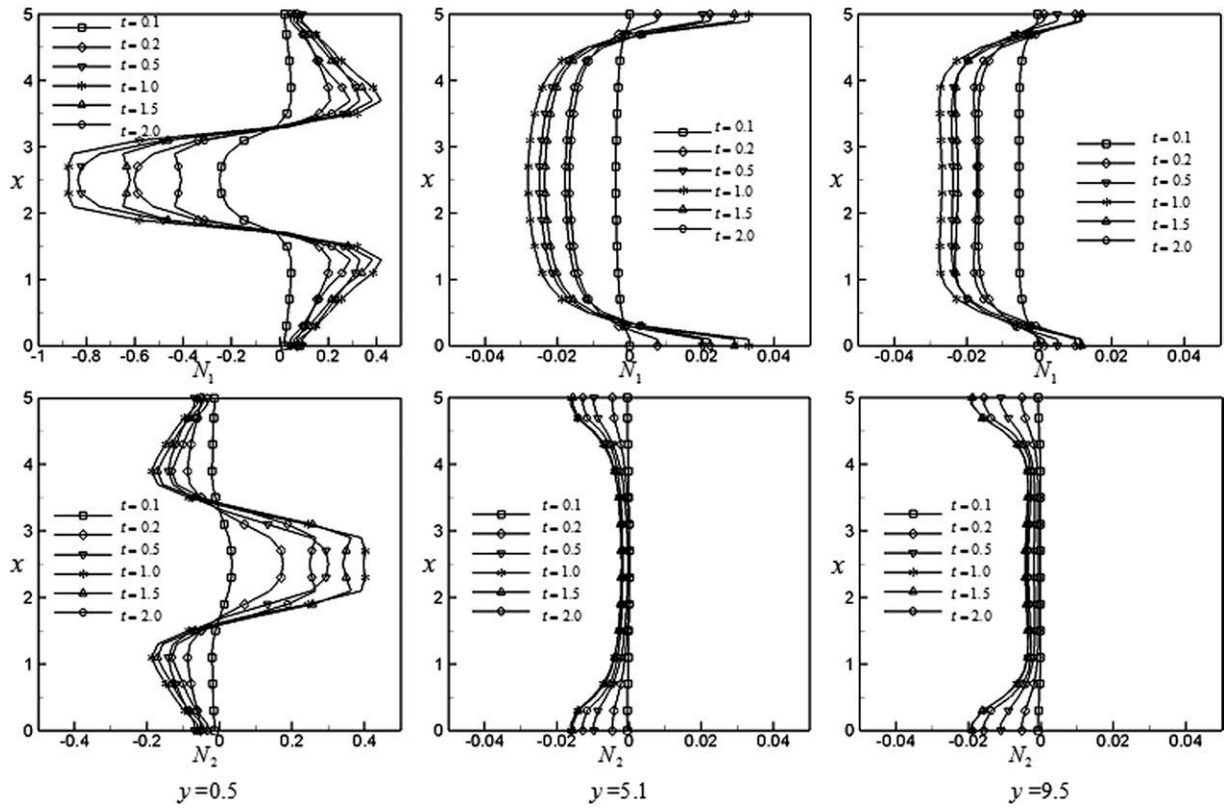

Figure 10 N_1 and N_2 profiles of the $z = 0.5$ midplane at different times and y values with We = 1.0 and $p_{\text{holding}} = 105$.

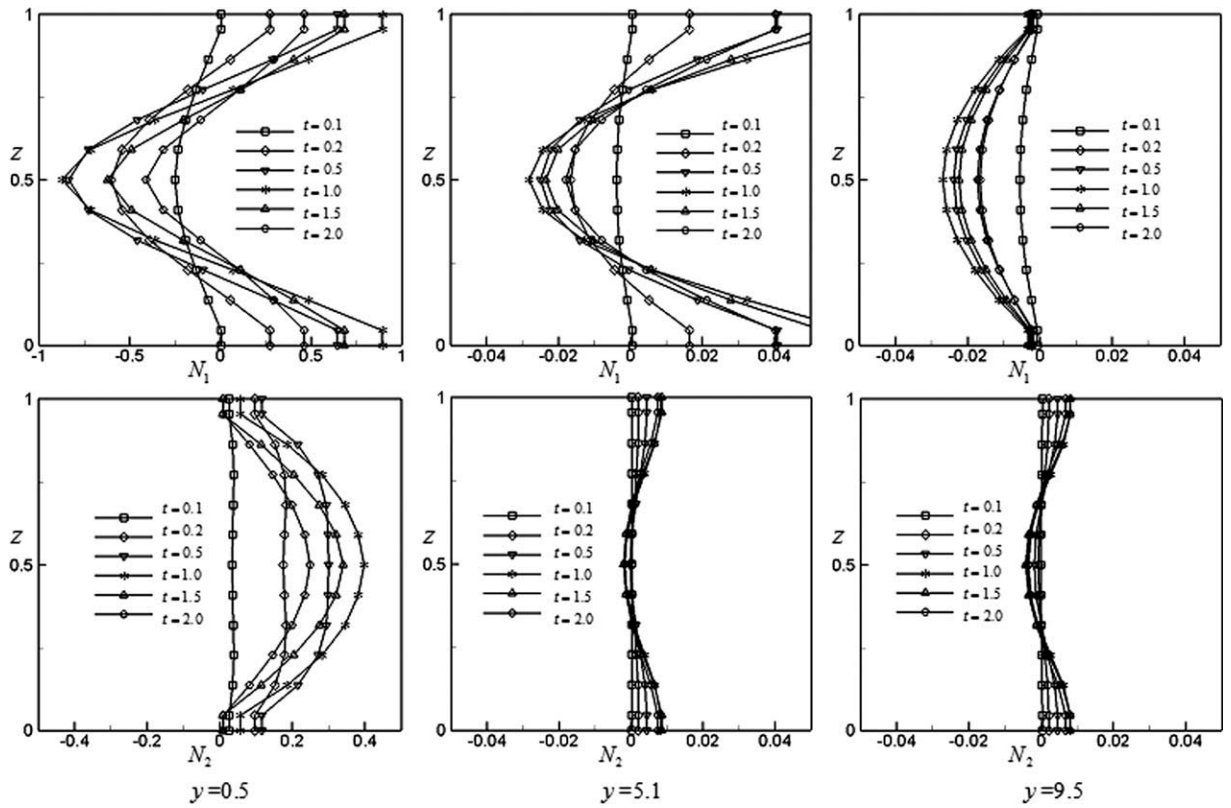

Figure 11 N_1 and N_2 profiles of the $x = 2.5$ midplane at different times and y values with We = 1.0 and $p_{\text{holding}} = 105$.

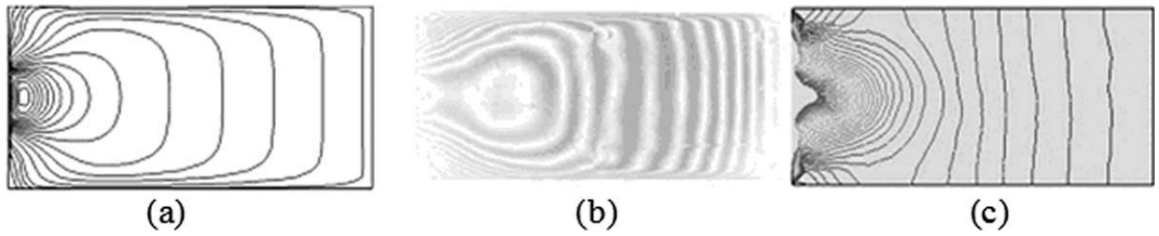

Figure 12 Comparisons among the calculated profiles of the flow-induced birefringence: (a) our results, (b) experimental results from ref. 8, and (c) numerical results from ref. 8.

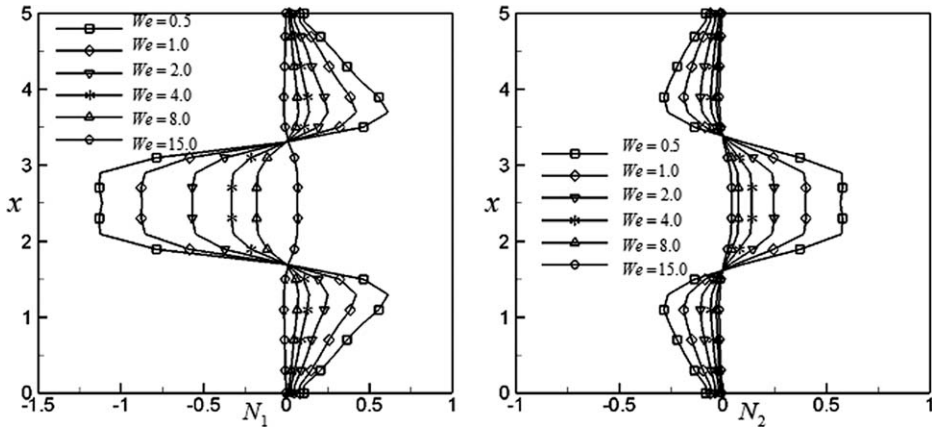

Figure 13 Influence of the elasticity on the N_1 and N_2 values at $t = 0.5$ with $z = 0.5$, $y = 0.5$, and $p_{holding} = 105$.

where Δn is the flow-induced birefringence, n_x and n_y are the refraction indices along the x- and y-axis directions, respectively; and C is the stress–optical coefficient of the polymer in the melt state. We assumed a constant linear stress–optical rule.

These numerical results of flow-induced birefringence, which were obtained according to the rule in eq. (41), are shown and compared with the experimental results (see ref. [8]) in Figure 12. The basic principle of the photoelasticity experiment is that when a ray of plane light passes through an anisotropic material, it experiences two different refractive indices; this difference leads to a relative retardation and shows up in a polariscope by way of a fringe pattern.

From Figure 12, it can be seen that the calculated results coincided well with the experimental results in tendency, especially for the position far away from the gate. Nevertheless, there was a small difference near gate because the gates were not completely the same.

Influence of the elasticity on the normal stress differences

The N_1 and N_2 profiles at $t = 0.5$ with $z = 0.5$, $y = 0.5$, $p_{holding} = 105$, and increasing We are shown in Figure 13. It can be seen that N_1 and N_2 were symmetric about the x-axis midline. From Figure 13, we see that the absolute values of N_1 and N_2 decreased as We increased. This tendency still helds at different positions, as shown in Table IV, which gives the N_1 and N_2 values at reference points P_1 and P_3 at $t = 0.5$ with $p_{holding} = 105$ and increasing We.

Influence of the holding pressure on the normal stress differences

Figure 14 shows the N_1 and N_2 values at $t = 0.5$ with $z = 0.5$, $y = 0.5$, We = 0.5, and different holding pressures. It can be seen that N_1 and N_2 were symmetric about the x-axis midline in Figure 14. Moreover, the holding pressure had a great influence on the normal stress differences near the gate

TABLE IV
Normal Stress Differences at Two Reference Points at t = 0.5 with We = 0.5 and Different Holding Pressures

	P_1		P_3	
P (10^4)	N_1	N_2	N_1	N_2
7	−0.8955	0.3604	−0.0301	0.0026
8	−1.0443	0.4110	−0.0338	−0.0029
10	−1.3447	0.5095	−0.0410	−0.0034
12	−1.6412	0.6035	−0.0481	−0.0039

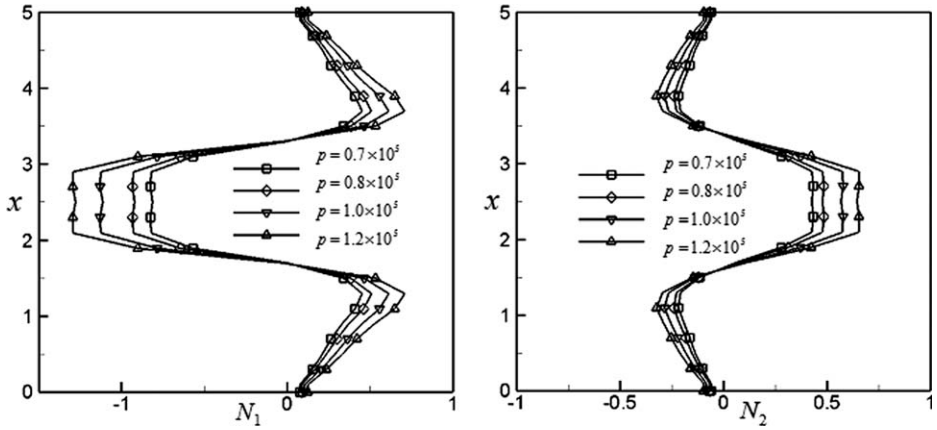

Figure 14 Influence of the holding pressure on the N_1 and N_2 values at $t = 0.5$ with $z = 0.5$, $y = 0.5$, and We = 0.5.

($y = 0.5$), and we could see clearly that as the values of holding pressure increased, the absolute values of N_1 and N_2 increased, too. This tendency still held at different positions, as shown in Table V, which gives the N_1 and N_2 values at reference points P_1 and P_3 at $t = 0.5$ with We = 0.5 and different holding pressures. Holding pressure increases can make a product's mass increase to decrease the shrinkage,[36] but it makes the flow-induced stress increase, so we must ensure appropriate holding pressure in the packing stage to improve the properties of products.

CONCLUSIONS

In this study, a numerical simulation of the full 3D packing process and flow-induced stresses was examined on the basis of the XPP model. A hybrid FEM–FVM was used to solve this model. The numerical results show that

1. The hybrid FEM–FVM could successfully solve the viscoelastic polymer melt flow model and simulate the viscoelastic stresses precisely by solving the benchmark problem.
2. The pressure values were digressive from the gate to the end of the cavity during the packing process. Finally, the pressure values reached holding pressure almost in the whole cavity, and the pressure value of the reference point near the gate reached the holding pressure earlier than those of other reference points.
3. The normal stress differences and each stress component were symmetric about the midline. The stress distributions showed the greatest differences near the gate, and the maximum value of the normal stress differences appeared near the gate, where there existed complex shear and normal forces. The absolute values of N_1 and N_2 decreased first and increased afterward with increasing time.
4. By comparison, the calculated flow-induced birefringence was in agreement with the experimental results in tendency.
5. The absolute values of the normal stress differences decreased with increasing We and increased with increasing holding pressure. The holding pressure and elasticity of the materials should be considered in the packing process to improve the properties of the products.

TABLE V
Normal Stress Differences at Two Reference Points at $t = 0.5$ with $p_{holding} = 105$ and Different We Values

	P_1		P_3	
We	N_1	N_2	N_1	N_2
0.5	−1.3447	0.5095	−0.04102	−0.003395
1.0	−0.8364	0.2999	−0.02386	−0.001892
2.0	−0.4721	0.1645	−0.01291	−0.001002
4.0	−0.2519	0.08644	−0.006723	−0.0005156
8.0	−0.1302	0.04436	−0.003431	−0.0002616
12.0	−0.08782	0.02984	−0.002303	−0.0001753
15.0	−0.07058	0.02395	−0.001847	−0.0001405

The numerical simulation of the flow-induced stresses of the packing process was achieved in this study. We hope that the results obtained have some valuable references to the actual production process for improving product quality. Because the existence of the change phase, in the future, we will consider the use of an enthalpy transforming model to deal with this problem for calculating the frozen-in stresses in plastic parts.

References

1. Hassan, H.; Regnier, N.; Pujos, C.; Defaye G. J Appl Polym Sci 2009, 114, 2901.
2. Harrison, P.; Janssen, L. J. P.; Peters, G. W. M.; Baaijens, F. P. T. Rheol Acta 2002, 41, 114.

3. Kim, C. H.; Kim, S.; Oh, H.; Youn, J. R. Fiber Polym 2007, 8, 443.
4. Hong, J. S.; Park, S. R.; Lyu, M. Y. Polym-KOREA 2011, 35, 1.
5. Frank, P. T. B.; Lucien, F. A. D. Appl Sci Res 1991, 48, 141.
6. Isayev, A. I.; Shyu, G. D.; Li, C. T. J Polym Sci Part B: Polym Phys 2006, 44, 622.
7. Yang, S. S.; Kwon, T. H. Korea-Aust Rheol J 2007, 19, 191.
8. Cao, W.; Shen, C. Y.; Zhang, C. J.; Wang, L. X. Arch Appl Mech 2008, 78, 363.
9. El Otmani, R.; Zinet, M.; Boutaous, M.; Benhadid, H. J Appl Polym Sci 2011, 121, 1579.
10. Gao, D. M.; Nguyen, K. T.; Hetu, J. F.; Laroche, D.; Garcia-Rejon, A. Adv Perform Mater 1998, 5, 43.
11. Cardozo, D. J Reinf Plast Compos 2008, 27, 1963.
12. Geng, T.; Li, D. Q.; Zhou H. M. Eng Comput 2006, 21, 289.
13. Yan, B.; Zhou, H. M. Li, D. Q. P I Mech Eng Part B: J Eng 2007, 221, 1573.
14. Zhou, H. M.; Yan, B.; Zhang, Y. J Mater Process Tech 2008, 204, 475.
15. Zhou, J.; Turng, L. S. Adv Polym Tech 2006, 25, 247.
16. Zhou, W.; Ouyang, J.; Yang, B. X.; Li, Q. CIESC J 2011, 62, 618.
17. Dantzig, J. A.; Tucker, C. L. Modeling in Materials Processing; Cambridge University Press: Cambridge, United Kingdom, 2001.
18. Zhou, H.; Zhang, Y.; Li, D. Proc Inst Mech Eng Part B 2001, 215, 1459.
19. Kang, S. Y.; Kim, S. K.; Lee, W. I. Int J Numer Meth Fluids 2008, 57, 139.
20. Verbeeten, W. M. H.; Peters, G. W. M.; Baaijens, F. P. T. J Rheol 2001, 45, 823.
21. Verbeeten, W. M. H.; Peters, G. W. M.; Baaijens, F. P. T. J Non-Newtonian Fluid Mech 2002, 108, 301.
22. Tang, H. S.; Sotiropoulos, F. Comput Fluids 2007, 36, 974.
23. King, R. C.; Apelian, M. R.; Armstrong, R. C.; Brown, R. A. J Non-Newtonian Fluid Mech 1998, 29, 147.
24. Rajagopalan, D.; Armstrong, R. C.; Brown, R. A. J Non-Newtonian Fluid Mech 1990, 36, 159.
25. Baaijens, F. P. T. J Non-Newtonian Fluid Mech 1998, 75, 119.
26. Hwang, W. R.; Walkley, M. A.; Harlen, O. J. J Non-Newtonian Fluid Mech 2011, 166, 354.
27. Wang, W.; Li, X. K.; Han, X. H. J Non-Newtonian Fluid Mech 2010, 165, 1480.
28. Aboubacar, M.; Aguayo, J. P.; Phillips, P. M.; Phillips, T. N.; Tamaddon-Jahromi, H. R.; Snigerev, B. A.; Webster, M. F. J Non-Newtonian Fluid Mech 2005, 126, 207.
29. Yang, B. X.; Ouyang, J.; Li, Q.; Zhao, Z. F.; Liu, C. T. J. Non--Newtonian Fluid Mech 2010, 165, 1275.
30. Boronat, T.; Segui, V. J.; Peydro, M. A.; Reig, M. J. J Mater Process Tech 2009, 209, 2735.
31. Chiang, H. H.; Hieber, C. A.; Wang, K. K. Polym Eng Sci 1991, 37, 116.
32. Nithiarasu, P.; Mathur, J. S.; Weatherill, N. P.; Morgan, K. Int J Numer Meth Fluids 2004, 44, 1207.
33. Guermond, J. L.; Minev, P. D. Commun Numer Meth Eng 2003, 19, 535.
34. Perron, S.; Boivin, S.; Herard, J Comput Fluids 2004, 33, 1305.
35. Edussuriya, S. S.; Williams, A. J.; Bailey, C. J Non-Newtonian Fluid Mech 2004, 117, 47.
36. Kwon, K.; Isayev, A. I.; Kim, K. H. J Appl Polym Sci 2005, 98, 2300.